Polaronic deformation at the $Fe^{2+/3+}$ impurity site in Fe:$LiNbO_3$ crystals

A. Sanson,* A. Zaltron, N. Argiolas, C. Sada, and M. Bazzan†
Dipartimento di Fisica e Astronomia, Università di Padova, via Marzolo 8, I-35131, Padova, Italy

W. G. Schmidt and S. Sanna‡
Lehrstuhl für Theoretische Physik, Universität Paderborn, 33095 Paderborn, Germany

(Received 2 December 2014; revised manuscript received 30 January 2015; published 17 March 2015)

Iron doped $LiNbO_3$ crystals with different iron valence states are investigated. An extended x-ray absorption fine structure (EXAFS) spectroscopy study highlights evident changes in the local structure around iron that can be ascribed to the presence of small polarons. In particular, when a Fe^{3+} replaced a Li ion, the oxygen octahedron shrinked with respect to the pure material, with an average iron-oxygen bond value very similar to that of Fe_2O_3 hematite. When adding an electron, it localizes at the Fe site in a configuration very close to the atomic Fe *d* orbitals, inducing a relaxation of the oxygen cage. The same system was modelled by spin-polarized density functional theory (DFT). Several local as well as hybrid exchange-correlation functionals were probed on the bulk $LiNbO_3$ structural properties. The computation is then extended to the case of hematite and finally to the Fe defect in $LiNbO_3$. The calculations reproduced with good accuracy the large lattice relaxation of the oxygen ligands associated to the electronic capture at the Fe center that can be interpreted as due to the polaron formation. The calculations reproduce satisfactorily the available EXAFS data, and allow for the estimation of the polaron energies and the optical properties of the defect.

DOI: 10.1103/PhysRevB.91.094109 PACS number(s): 71.38.−k, 61.05.cj, 31.15.A−, 77.84.−s

I. INTRODUCTION

Lithium niobate is a widely employed optical material due to its excellent electro-optical and nonlinear optical properties. In particular, upon inhomogeneous illumination in the visible range, photoexcitation of movable charges can give rise to a space charge redistribution and, consequently, to the building up of an electric field. The latter induces a refractive index modulation by the electro-optic effect, a phenomenon usually referred to as photorefractivity. Thanks to this property, lithium niobate crystals ($LiNbO_3$, LNB) were exploited to realize optical data storage stages via holographic recording [1] as well as holographic filters, demultiplexers, optical memories, and phase-conjugated mirrors [2,3]. More recent applications include the development of compact and multipurpose optical sensors for environment and bio-chemical applications [4,5]. In literature, the physical phenomena underlying photorefractivity are commonly described by photoexcitation of electrons from the material donor centers into the conduction band [2]. In this picture, the diffusion, photovoltaic, and drift mechanisms allow the photo-excited electrons to redistribute in the material and be trapped in acceptor centres: the most common donor/acceptor centers in this material are the extrinsic Fe^{2+}/Fe^{3+} impurities as well as the intrinsic Nb^{+4}/Nb^{5+} centers [6–9]. Consequently, the photorefractive response can be easily enhanced and tailored, with intentional iron doping of the pure material (Fe:$LiNbO_3$) and with an accurate control of the Fe concentration together with its valence state. More recently, it became clear that due to the strong electron phonon coupling occurring in LNB, charge transport in this material has to be described in terms of photoexcitation and diffusion of small polarons [10,11]. These quasiparticles consist of an electric charge that is able to localize by deforming the surrounding lattice, thus creating a temporary potential well. The term *small* means that this lattice deformation extends on the length of about one unit cell. Under certain conditions, the charge and the deformation can move as a whole by thermally activated hopping [12,13], and eventually be trapped by crystal defects and impurities. In LNB, doped with Fe for photorefractive applications, at least four polaron types have been recognized [10]: (a) free electron polarons localizing at Nb ions; (b) bound electron polarons localizing at Nb_{Li} antisite defects, always present in congruent material; (c) bound hole polarons, localizing at O ions; and (d) bound electron polarons localized at the Fe impurities. In order to deal adequately with the features of these charge carriers in the numerous possible photorefractive applications of Fe:LNB, it is essential to understand their structure, especially by quantitative studies. This work is devoted to the investigation of the Fe polaron in LNB. Generally, polarons in LNB are indirectly investigated by their impact on the optical and/or transport properties, in the framework of a simple phenomenological model, which describes the polaron formation as a balance between the elastic energy paid to deform the lattice and the electrostatic energy gained by the charge in the newly formed localization potential [13]. Unfortunately, the simultaneous determination of all the parameters entering this model (primarily the total polaron energy, the energy stored in the elastic deformation, and the defect binding energy) can be determined only by a comparison with experimental data [10], which are not always known or difficult to obtain, especially for bound polarons. Moreover, the details of the electronic and local crystal structure of this defect remain out of reach.

Quite surprisingly, there exist few experimental and theoretical studies reporting on the direct investigation of the most basic characteristics of the Fe bound polaron, i.e., the local distortion produced by the self-trapping action and its

*andrea.sanson@unipd.it
†marco.bazzan@unipd.it
‡simone.sanna@uni-paderborn.de

electronic structure. Generally, the incorporation of Fe in LNB was experimentally studied only from the point of view of lattice site location and determination of the Fe valence state [14–24]. However, some recent XRD results [25] showed that the electron capture by the Fe center produces a strain in the crystal matrix, indicating the onset of a measurable deformation at the Fe centers when their valence is changed from Fe^{3+} to Fe^{2+} by a reduction treatment. This suggests that a *direct* measure of the deformation associated to the Fe polaron formation should be possible. In order to interpret these results, theoretical *ab initio* methods could be used. This approach would therefore complement phenomenological modeling by obtaining from first principles the unknown quantities of the system. By comparing experimental data with a systematic tuning of the different approximation schemes, it should be possible to determine those calculations which best reproduce the experimental data and subsequently use them to calculate the unknown quantities of the system. To our knowledge, *ab initio* studies on the Fe impurity in LNB published up to now [26] are limited to the investigation of the stability and lattice location of Fe^{2+} and Fe^{3+} defects and defects clusters in LNB using a DFT + U approach. The polaron problem, i.e., the change in the local structure associated to the capture of an electron by a Fe^{3+} center was not discussed.

The aim of the present paper is therefore to obtain a direct measure of the polaronic distortion at the Fe center and to compare the obtained results with accurate DFT + U *ab initio* calculations. A series of samples with high Fe concentration were prepared in fully oxidized and reduced states, so that all of the Fe ions present in the different samples can be considered to be either in their Fe^{3+} or Fe^{2+} state, respectively. The local structure around Fe impurity was then investigated by extended x-ray absorption fine structure (EXAFS) spectroscopy and the differences, ascribed to the polaron formation, obtained. These results were compared with a series of *ab initio* calculations, in order to test different approximation schemes and to reproduce and rationalize the polaronic deformation.

The paper is structured as follows: the sample preparation and characterization together with the experimental details are given in Sec. II; Sec. III reports the EXAFS data analysis; Sec. IV describes the computational study of models representing bulk $LiNbO_3$, α-Fe_2O_3 and Fe_{Li} substitutionals in $LiNbO_3$. Finally, a discussion and conclusions of this combined investigation are provided in Sec. V.

II. EXPERIMENTAL DETAILS

A. Sample preparation and characterization

One boule of iron doped lithium niobate (Fe:$LiNbO_3$) with congruent composition was grown at the University of Padova by using the Czochralski technique. The dopant concentration in the melt was [Fe] = 188.55×10^{18} cm^{-3} = 1% mol and the growth direction was along the z axis of the material, with a pulling rate of 1 mm/h. After the growth, the Fe:$LiNbO_3$ boule was poled in air atmosphere at 1200 °C in order to obtain a single domain structure. The boule was thereafter x-ray oriented and cut in different slab samples with the main face perpendicular to the z axis of the material (z cut). Finally, the samples were polished to achieve a good optical quality.

Subsequently, one sample has been treated in a gas mixture of Ar(98%)+H2(2%) at 500 °C, with a flux of 100 Nl/h for 40h, thus promoting the incorporation of electrons inside the material and consequently the reduction of Fe^{3+} ions into Fe^{2+}. A second sample has been annealed O_2 atmosphere (90 Nl/h) at 900 °C for 20h. These two samples in the following will be referred to as Fe^{2+} :LNB (reduced) and Fe^{3+} :LNB (oxidized), respectively, and correspond ideally to the cases of a sample containing only filled Fe^{2+} polaronic centers and another containing empty Fe^{3+}.

One of the main macroscopic evidences of this reduction process is a modification of the optical absorption of the material, related to excitation of Fe^{2+} polarons. Indeed, reduced Fe:$LiNbO_3$ shows two wide absorption bands centered at 2.6 eV (D band) and 1.1 eV (A band), whose intensities are proportional to the Fe^{2+} polarons concentration [10]. To check the content of Fe^{2+} and Fe^{3+} present in each sample, optical absorption measurements were performed in transmission mode by using a Jasco V-670 spectrophotometer in the range 300–2700 nm. Usually, in literature the optical absorption at 477 and 532 nm is used to determine the concentration of filled traps in the material [22,23,27], but in our case the absorption at the mentioned wavelengths is too high to be properly measured even in a slightly reduced crystal, due to the high amount of dopant present in the material. We therefore exploited the absorption cross section of Fe^{2+} at 1128 nm (A band) [27,28], which is equal to $(0.32 \pm 0.01) \times 10^{-18}$ cm^2. The concentration of Fe^{3+} and Fe^{2+} ions relative to the investigated samples is listed in Table I, where it is possible to notice that in the oxidized sample Fe is mainly in its 3+ valence state, whereas in the reduced crystal the Fe traps have been almost completely filled.

B. EXAFS measurements

EXAFS spectroscopy is a powerful tool for studying the local structure and dynamics of materials [29–32]. In this work, Fe- $LiNbO_3$ was investigated by Fe K edge EXAFS measurements performed in fluorescence mode between 30 and 400 K at the BM23 XAS beamline of the European Synchrotron Radiation Facility (ESRF) in Grenoble (France). The storage ring was operated with an electron energy of 6 GeV and a typical current of 190 mA. The oxidized and

TABLE I. Concentrations of empty and filled traps present in the Fe:$LiNbO_3$ samples investigated in this work and corresponding reduction degrees. The experimental parameters used during the oxidizing/reducing thermal treatments are also reported.

Sample	Thermal treatment	Fe^{2+} ($\times 10^{18}$ cm^{-3})	Fe^{3+} ($\times 10^{18}$ cm^{-3})	Fe^{2+}/Fe^{3+}
Fe^{3+} :LNB	O_2 dry (900 °C, 20h)	≈2	186.4 ± 3.1	≈0.01
Fe^{2+} :LNB	Ar + H_2 dry (500 °C, 40h)	156.9 ± 6.4	31.7 ± 6.4	5.0 ± 0.2

reduced samples have been cut in two halves: one part was kept as reference for further compositional and structural characterizations, whereas the second part was finely ground. The samples for EXAFS were prepared by mixing and pelletizing the Fe- $LiNbO_3$ powders with boron nitride powder. The absorption coefficient was measured from 6900 to about 8000 eV by selecting the iron K α emission making use of a 13 elements high-purity Ge detector. An energy step varying from about 0.3 eV in the near-edge region to 4 eV at the highest energies was used, so to have a uniform wave vector step $\Delta k \simeq 0.03$ Å^{-1} in the EXAFS region. A Si(111) double crystal monochromator was used to monochromatize the x-ray beam, and a pair of Si mirrors at grazing incidence of 3.5 mrad was employed to reduce the effect of harmonics. The samples were mounted in a liquid helium cryostat and the temperature was stabilized and monitored through an electric heater controlled by a feedback loop, ensuring a thermal stability within ± 1 K. At least three spectra were collected at each temperature to allow an evaluation of experimental uncertainty, with an acquisition time of 4 s/point. Fine powders of α-Fe_2O_3 were also measured in transmission mode and used as standard reference for our experiment.

III. EXAFS DATA ANALYSIS AND RESULTS

Let us recall that the EXAFS signal of one coordination shell can be parameterized in terms of one-dimensional distribution $\rho(r)$ of interatomic distances through the cumulant expansion method, i.e.,

$$\chi(k) = \frac{S_0^2}{k} N |f(k,\pi)| \frac{e^{-2C_1/\lambda}}{C_1^2} e^{-2k^2C_2+2k^4C_4/3+\cdots} \times \sin[2kC_1 - 4k^3C_3/3 + \cdots + \phi(k)], \quad (1)$$

where S_0^2 is the amplitude reduction factor taking into account intrinsic inelastic effects, N is the coordination number, λ the photoelectron mean free path, $f(k,\pi)$ and $\phi(k)$ are the backscattering amplitude and total phase shift, respectively [29,33,34]. Equation (1) expresses EXAFS as a function of the cumulants C_i of an effective pair distribution $P(r,\lambda) = \rho(r)\exp(-2r/\lambda)/r^2$, where the first cumulant C_1 measures the mean value of the distribution, the second cumulant C_2 the variance, and the third cumulant C_3 the asymmetry. However, one is interested in the corresponding cumulants C_i^* of the real distribution of distances $\rho(r)$. In this regard, it can be shown that the difference between the second and higher-order cumulants of the two distributions can be neglected for not-highly disordered systems, while the first cumulants C_1^* and C_1 are connected through equation [35]

$$C_1^* = C_1 + \frac{2C_2}{C_1}\left(1 + \frac{C_1}{\lambda}\right). \quad (2)$$

After pre-edge subtraction and normalization of the experimental absorption coefficients, the photoelectron wave vector k was calculated with respect to the energy edge usually set at the maximum of the first derivative of the spectrum. For each of the two Fe^{3+} :LNB and Fe^{2+} :LNB samples, the energy axes of all spectra were shifted to achieve the best alignment with the lowest-temperature spectrum in the edge region and the edge energy of each spectrum was determined accordingly. The maximum energy shift was found to be about 0.1 eV between spectra of the same sample, thus proving the excellent stability of the energy axis. Differently, the energy edge of the Fe^{2+} :LNB sample is shifted towards lower energies of about 3 eV with respect to the Fe^{3+} :LNB sample. This is expected and due to the different valence state of iron [36,37].

In the following, it is assumed that Fe is incorporated into an axial-symmetric position inside the oxygen cage normally occupied by a Li ions, in accordance with the published literature [14–21,38]. In this picture the Fe ion is surrounded by six oxygens, in a configuration very close to the hematite (α-Fe_2O_3) structure. In ferroelectric lithium niobate, the oxygen octahedron is slightly distorted so that, assuming that the Fe exactly replaces the Li ion in an axial symmetric position and that the lattice structure remain unchanged with respect to perfect LNB, there are two possible lengths for the Fe-O bonds. In other words, three among the six oxygens composing the octahedron lie slightly closer to the Fe center than the others. The published studies on the Fe polaron in LNB are based on this configuration [10,11].

Two independent analysis procedures were used to obtain quantitative information. The first procedure is based on the so-called "ratio method" [33,39]: it consists of a separate analysis of amplitude and phase of the filtered EXAFS signal, taking the spectrum of α-Fe_2O_3 as reference for backscattering amplitudes, phase shifts, and inelastic terms. In this analysis, the difference between the two Fe-O lengths is neglected, as if Fe was equidistant from the oxygen and nearest-neighbor distances are assumed to follow one single-peaked distribution. With this method it is therefore possible to determine the "average" variation of the bond lengths when the polaron is formed. In the second and more detailed procedure, backscattering amplitudes, phase shifts and inelastic terms are theoretically calculated by the FEFF code [40] and the best fit of the experimental data are then made by the FEFFIT program [41]. This last approach allows to separate the two different nearest-neighbors Fe-O distances, as was recently done in α-Fe_2O_3 [42]. The consistency between the results of the two methods (see below) demonstrates the quality of our analysis.

A. Ratio method

By equation (1), one can see that having a proper reference spectrum, the difference between the EXAFS phases and the logarithm of the amplitude ratio can be written as

$$\Phi_s(k) - \Phi_r(k) = 2k\Delta C_1 - \tfrac{4}{3}k^3\Delta C_3 + \cdots \quad (3)$$

and

$$\ln\frac{A_s(k)}{A_r(k)} = \ln\frac{N_s}{N_r} - 2k^2\Delta C_2 + \frac{2}{3}k^4\Delta C_4 + \cdots \quad (4)$$

where ΔC_n indicates the cumulant difference $C_{n,s} - C_{n,r}$ and the subscripts s and r refer to the sample and reference (α-Fe_2O_3 at room temperature in this work), respectively. Thanks to this procedure the unknown quantities $|f(k,\pi)|$, $\phi(k)$ and S_0^2 in Eq. (1) are canceled.

The left panels of Fig. 1 show the k-weighted EXAFS signals $k\chi(k)$ of the two samples and of the reference. The structure of the EXAFS spectra obtained from the two samples

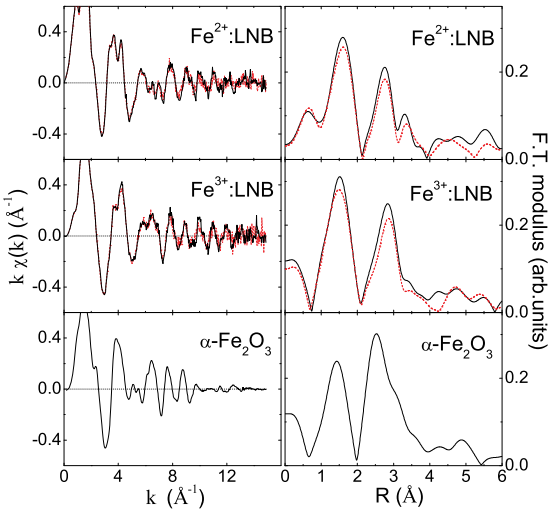

FIG. 1. (Color online) Fe K-edge EXAFS signals $k\chi(k)$ (left) and corresponding Fourier transform (right) adopted in the ratio method analysis. Top, middle, and bottom panels refer to Fe^{2+} :LNB, Fe^{3+} :LNB and reference α-Fe_2O_3, respectively. The black-solid and red-dashed lines refer to 30 K and room temperature, respectively.

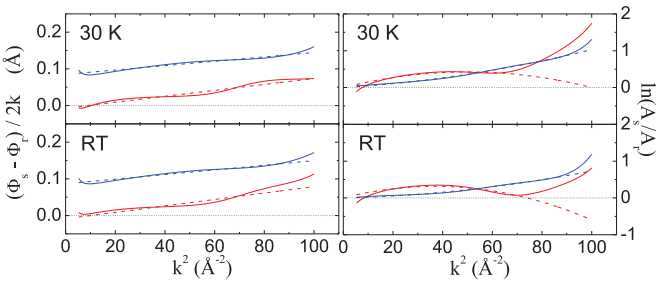

FIG. 2. (Color online) Phase differences (left) and logarithms of amplitude ratios (right) plotted against k^2 for two selected temperatures: 30 K (upper) and room temperature (lower). Blue and red lines refer to Fe^{2+} :LNB and Fe^{3+} :LNB, respectively. α-Fe_2O_3 at room temperature was used as reference. Dashed-lines are the corresponding best-fit curves.

appear qualitatively different, confirming that the electron capture process lead to a distortion of the local structure. In this first analysis, performed by using the EXTRA code [43], the EXAFS signals were extracted by the same polynomial spline for all spectra, best fitting the average behavior of the absorption coefficient. Then, in order to separate the contributions of the different coordination shells, the EXAFS signals were Fourier transformed (FT) in the interval $k = 2.3$–12 Å^{-1} with a k weighting and a 10% Gaussian window, as shown in the right panels of Fig. 1.

The peak centered at about 1.5 Å in the FT is due to the six nearest-neighbor oxygen atoms around Fe, forming a distorted FeO_6 octahedron, while the structure between about 2 and 3.5 Å contains several single and multiple scattering contributions. The FT structure below about 0.7 Å is probably due to a low-frequency component that remains in the spectrum after background subtraction. However, it could also be due to atomic XAFS [44,45] and, therefore, we cannot state with absolute certainty that this low R component in the FT has not a physical meaning, also for the fact that different polynomial splines were tested to remove it but with no success. To remove such FT component at low R the AUTOBK code [46] may be used, as will be done by FEFF-FEFFIT analysis in the next subsection. Nevertheless, also the background obtained by AUTOBK can be affected by spurious oscillations, in particular near the absorption edge, due to the forced removal of the low R component. Accordingly, we cannot know with certainty which background is better, although the one from AUTOBK probably is. As a result, we used both backgrounds in two different analyses (ratio method and FEFF-FEFFIT). The convergence of the results (see below) demonstrates that both methods are sufficiently sound and reliable, at least within our experimental uncertainties.

The first-peak contribution of Fig. 1 was singled out by Fourier back-transform. Then, according to Eqs. (3) and (4), the phase differences and logarithms of amplitude ratios were calculated and plotted against k^2 (see Fig. 2), taking the α-Fe_2O_3 spectrum as reference for backscattering amplitudes, phase shifts, and inelastic terms. The ratio method allows a visual evaluation of the overall quality of experimental data and of the useful k range which, in our case, is limited to the interval $k \simeq 3$–9 Å^{-1} or less. In the phases plot (left panels of Fig. 2), the vertical intercept is ΔC_1 with respect to the reference α-Fe_2O_3, while the linear slope is proportional to the third cumulant variation ΔC_3. It emerged that the average Fe-O distance in Fe^{2+} :LNB is almost 0.1 Å longer than in α-Fe_2O_3, while it is about the same in Fe^{3+} :LNB. In the amplitudes plot (right panels of Fig. 2) the linear slope is proportional to the variation of the second cumulant ΔC_2 (since the coordination number is constant, the intercept $\ln N_s/N_r$ was fixed to zero). A deviation from linearity indicates the relevance of the fourth cumulant ΔC_4

The average Fe-O bond distance (C_1^*) determined from EXAFS is shown in Fig. 3 for both Fe^{2+} :LNB and Fe^{3+} :LNB compounds at different temperatures. The values for C_1^* were

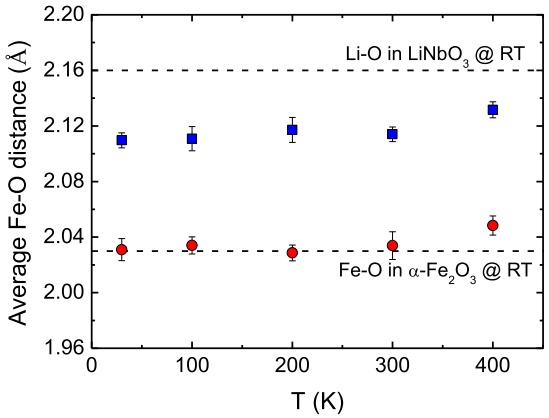

FIG. 3. (Color online) Average Fe-O distance determined from the ratio method in Fe^{2+} :LNB (blue squares) and Fe^{3+} :LNB (red circles) compounds. The dashed lines at about 2.03 and 2.16 Å refer to the average Fe-O and Li-O distances in α-Fe_2O_3 and $LiNbO_3$, respectively. The error bars were calculated as standard deviation over the different spectra and fitting intervals.

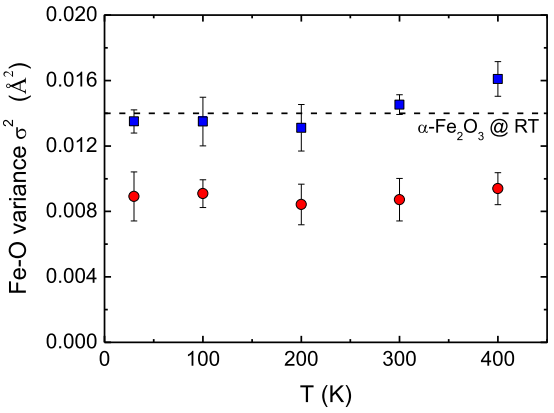

FIG. 4. (Color online) Variance σ^2 of the average Fe-O distance distribution determined from the ratio method in Fe^{2+} :LNB (blue squares) and Fe^{3+} :LNB (red circles) compounds. The dashed line at 0.014 Å refer to the Fe-O variance of α-Fe_2O_3 at room temperature. The error bars were calculated as standard deviation over the different spectra and fitting intervals.

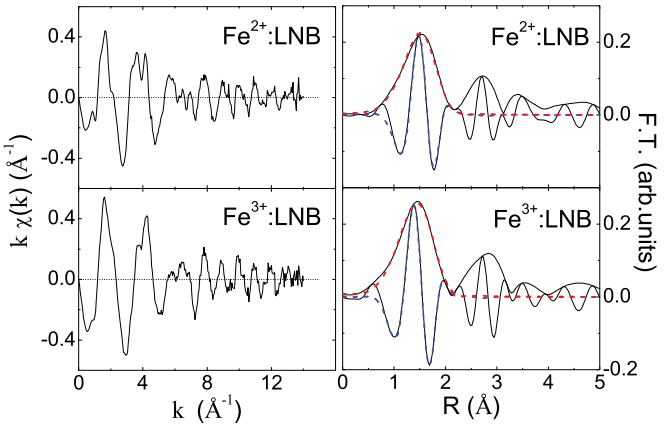

FIG. 5. (Color online) (Left) Fe K-edge EXAFS signals $k\chi(k)$ extracted by AUTOBK and adopted in the FEFF-FEFFIT analysis. (Right) Modulus and imaginary part of the Fourier transform of the EXAFS signal (continuous lines) and best-fitting simulation of the first peak (colored dashed-bold lines). Top and bottom panels refer to Fe^{2+} :LNB and Fe^{3+} :LNBat 30 K, respectively.

calculated through Eq. (2), making use of the experimental ΔC_2 values and assuming $\lambda = 8$ Å (the error due to the exact value of λ, typically between 6 and 12 Å, does not exceed 0.001 Å), and through the comparison with the reference α-Fe_2O_3, whose average Fe-O distance is ∼2.03 Å (three short Fe-O distances at ∼1.94 Å + three long Fe-O distances at ∼2.12 Å) [47,48]. Figure 3 is a first clear experimental evidence of the polaron effect: the transformation from Fe^{3+} to Fe^{2+} relaxes the oxygen octahedron which becomes larger so that the average Fe-O distance passes from ∼2.03 Å in oxidized sample to ∼2.12 Å in reduced one (by comparison, the average Li-O distance in undoped LNB is ∼2.16 Å). This is consistent with ionic radii of octahedrally choordinated Li^+ ions (0.90 Å) and octahedrally choordinated Fe^{2+} (0.75 Å) and Fe^{3+} (0.69 Å). Those results are also in qualitative agreement with Ref. [25] which indicated a negative strain in oxidized Fe:$LiNbO_3$ films which was partially released by reducing the sample. Note that the average Fe^{3+} –O distance in Fe^{3+} :LNB is very similar to that of α-Fe_2O_3, where the valence state of iron (+3) is the same.

Figure 4 shows the variance (σ^2) of the average Fe-O distance distribution, measured by the second cumulant C_2^* of EXAFS, for Fe^{2+} :LNB and Fe^{3+} :LNB. The absolute value for C_2^* was determined by the comparison with α-Fe_2O_3, whose σ^2 at room temperature is estimated to be about 0.014 $Å^2$. This value is calculated as follows, taking into account both static and dynamic effects to the local disorder [49]. The contribution of static disorder (here denoted σ_s^2) to σ^2 was approximately calculated by considering the difference in the two nearest-neighbors Fe-O distances in hematite, $R_1 \simeq 1.94$ Å and $R_2 \simeq 2.12$ Å, thus getting $\sigma_s^2 = [(R_2 - R_1)/2]^2 \simeq 0.008$ $Å^2$. The dynamic contribution (here denoted σ_d^2) was instead determined as $\sigma_d^2 = (\sigma_{d1}^2 + \sigma_{d2}^2)/2$, where $\sigma_{d1}^2 \simeq 0.0043$ $Å^2$ and $\sigma_{d2}^2 \simeq 0.0075$ $Å^2$ are the vibrational contribution of each of the two nearest-neighbors Fe-O distances derived from Fig. 4 of Ref. [42]. The result is $\sigma_d^2 \simeq 0.006$ $Å^2$ and therefore $\sigma^2 = \sigma_s^2 + \sigma_d^2 \simeq 0.014$ $Å^2$.

B. FEFF-FEFFIT method

In this second analysis, we aim to distinguish the two sets of nearest-neighbors Fe-O distances in Fe^{2+} :LNB and Fe^{3+} :LNB sample, as was recently done for α-Fe_2O_3 [42].

Differently from the previous analysis by the ratio method: (i) the backscattering amplitude $|f(k,\pi)|$ and the total phase shift $\phi(k)$ of each of the two Fe-O distances are calculated by FEFF code [40]. This was performed by replacing a Li atom with a Fe atom in the crystal structure of $LiNbO_3$. (ii) To remove the FT component at low R, the AUTOBK code [46] was utilized to extract the EXAFS signals. (iii) The $k\chi(k)$ EXAFS signals were Fourier transformed in the range $k =$ 3–9 $Å^{-1}$, i.e., where, according to Fig. 2, the overall quality of the experimental data seems to be better.

The EXAFS signals $k\chi(k)$ of the two Fe^{2+} :LNB and Fe^{3+} :LNB compounds at 30 K, extracted by AUTOBK, are shown in the left panels of Fig. 5. Pronounced differences with respect to the EXAFS signals of Fig. 1 are evident at low k, thus confirming the fact that the FT structure at low R of Fig. 1 is due to how the background is extrapolated near the absorption edge. The modulus and imaginary part of the corresponding Fourier transform are shown by continuous lines in the right panels Fig. 5.

A nonlinear best-fit of the experimental spectra was performed in the r space between 0.6 and 2.1 Å (right panels of Fig. 5) by using the FEFFIT program [41]. No quantitative analysis of the second FT peak was attempted because, according to the FEFF calculation [40], a large number of scattering-paths are involved (about 10) and, moreover, because the part of the second-peak EXAFS signal related to first neighbors through the multiple scattering is small, only ∼18% or less of the total signal. As a consequence, the analysis of the second FT peak is not important to gain information on the two nearest-neighbor Fe-O distances and, accordingly, it has been omitted.

The number of free fitting parameters, i.e., E_0 (edge energy mismatch between theory and experiment), S_0^2 (amplitude reduction factor due to intrinsic inelastic effects), and the first

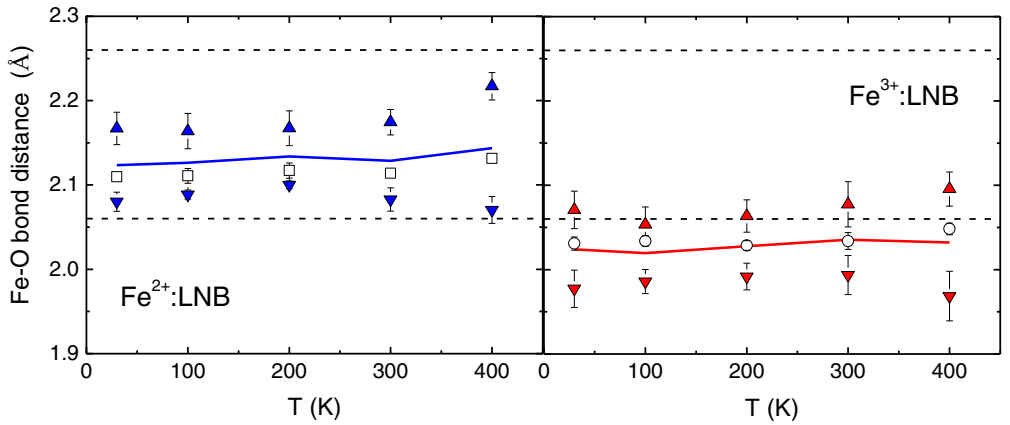

FIG. 6. (Color online) Short and long Fe-O bond distances (down and up triangles, respectively) determined by FEFF-FEFFIT analysis in Fe^{2+} :LNB (left) and Fe^{3+} :LNB (right) samples. The average of the two Fe-O distances (solid lines in each panel) is in agreement with the average Fe-O distance obtained by the ratio method (open symbols) in Sec. II A. The dashed lines indicate the short and long Li-O bond distances in pure $LiNbO_3$ at about 2.06 and 2.26 Å, respectively.

two cumulants for each of the two Fe-O distances, was reduced as much as possible. In a first trial analysis, the value of E_0 was left free and exhibited relatively small variations as a function of temperature (between −9.2 and −7.8 eV for Fe^{2+} :LNB, between −10.4 and −8.6 eV for Fe^{3+} :LNB). Then the average values of E_0 were calculated (about −8.3 eV for Fe^{2+} :LNB, −9.5 eV for Fe^{3+} :LNB) and kept fixed in the subsequent fitting procedure. To further reduce the uncertainty and the scattering of the results, the value of S_0^2 (strongly correlated with the second EXAFS cumulant) was fixed at different values within the typical range from 0.85 to 1.10, and the final results were then obtained as the average over all fitting runs. The uncertainties of each individual fit were those given by FEFFIT. The final error bars were then calculated according to the standard propagation of errors.

The resulting distance of the short and long Fe-O bonds, $Fe\text{-}O_1$ and $Fe-O_2$ respectively, are shown in Fig. 6 for both Fe^{2+} :LNB and Fe^{3+} :LNB samples. It can be observed that when Fe^{2+} replaces the Li ion, the surrounding oxygen cages shrink with respect to the pure LNB crystal, so that the two types of Fe-O distances become about 2.08 and 2.18 Å, respectively (left panel of Fig. 6). A further shrinking of the oxygen octahedra is observed when Li is substituted by Fe^{3+}. In this case the two Fe-O distances decrease up to about 1.98 and 2.07 Å, respectively (right panel of Fig. 6). Note that if the two Fe-O distances obtained through the present FEFF-FEFFIT analysis are averaged (solid lines), the resulting distances are in full agreement with those previously determined by the ratio method (open symbols) at all temperatures.

Figure 7 shows the second cumulant for the short and long Fe-O distances in Fe^{2+} :LNB and Fe^{3+} :LNB crystals (left and right panels, respectively). It corresponds to the variance of each distance distribution and, since the short and long distances have been separated, is entirely due to the thermal disorder. In order to compare, these results with the total σ^2 achieved by the ratio method in the previous subsection, let us denote with R_1 and R_2 the $Fe\text{-}O_1$ and $Fe\text{-}O_2$ distances of Fig. 6, respectively, and with σ_{d1}^2 and σ_{d2}^2 the corresponding variances shown in Fig. 7 due to thermal effects. Similarly to what was done for the reference $\alpha\text{-}Fe_2O_3$, we can calculate

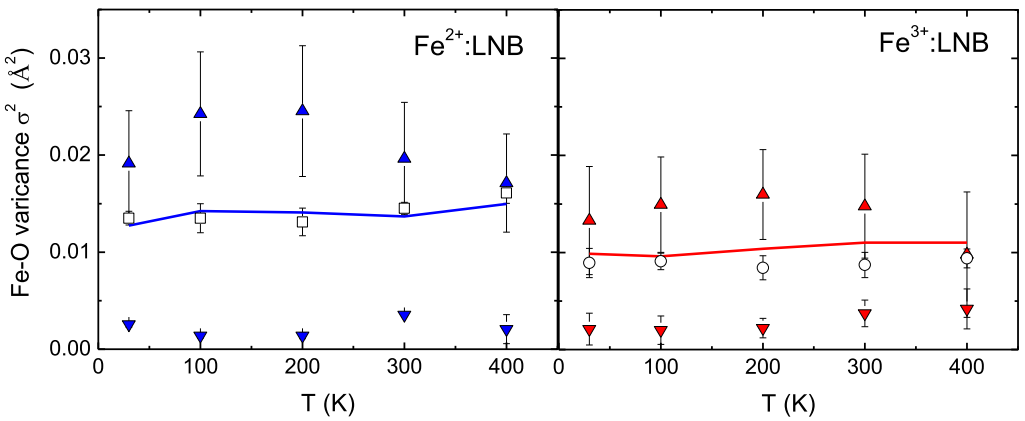

FIG. 7. (Color online) Variance σ_d^2 of the short and long Fe-O bond distances (down and up triangles, respectively) determined by FEFF-FEFFIT analysis in Fe^{2+} :LNB (left) and Fe^{3+} :LNB (right) crystals. The total variance σ^2 (solid lines in each panel, calculated by considering the static disorder σ_s^2 due to the two different Fe-O distances of Fig. 6) is in agreement with that obtained by the ratio method (open symbols) in Sec. II A.

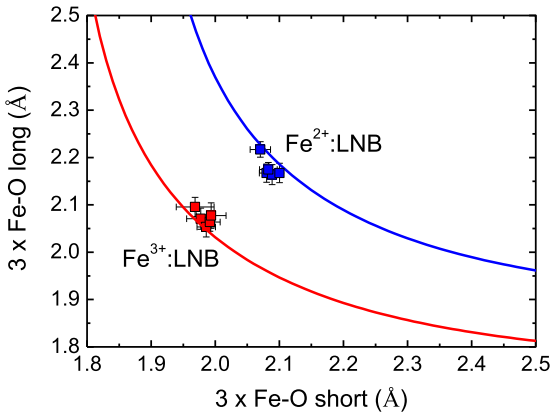

FIG. 8. (Color online) Long vs short Fe-O bond distance predicted by the bond valence model in Fe^{2+} :LBN (blue line) and Fe^{3+} :LBN (red line) compounds. Square symbols refer to the experimental distances determined by EXAFS (i.e., triangles in Fig. 6.)

the total σ^2 as $\sigma_s^2 + \sigma_d^2$, where $\sigma_s^2 = [(R_2 - R_1)/2]^2$ is the static contribution and $\sigma_d^2 = (\sigma_{d1}^2 + \sigma_{d2}^2)/2$ is the dynamic contribution. The resulting σ^2, for both Fe^{2+} :LNB and Fe^{3+} :LNB, is shown in Fig. 7 by solid lines. The agreement with the total σ^2 determined by the ratio method (open symbols in Fig. 7) is very good, and this proves again the reliability of our EXAFS results.

C. The bond-valence model

Before passing to the next section, we discuss the EXAFS results in the framework of the bond valence model [50–52]. This model, widely used in solid-state chemistry, expresses the valence V_i of a cation i as

$$V_i = \sum_j S_{ij}, \tag{5}$$

where the sum is over all the bonds of the cation with the anions j, and the bond valences S_{ij} are given by expression

$$S_{ij} = e^{(R_0 - r_{ij})/b}, \tag{6}$$

where b is commonly taken to be a constant equal to 0.37, r_{ij} is the bond length and R_0 is the bond-valence parameter. Once known, the most common applications in crystallography are in predicting bond lengths and in checking the reliability of a determined structure [51,52].

According to Ref. [50], the bond-valence parameter R_0 is 1.734 for the pair of atoms Fe^{2+}-O, 1.759 for the pair Fe^{3+}-O. Therefore, denoting by R_1 and R_2 the short and long Fe-O bond lengths, respectively, R_1 and R_2 should satisfy the relation

$$3e^{(1.734-R_1)/0.37} + 3e^{(1.734-R_2)/0.37} = +2 \tag{7}$$

in the case of Fe^{2+} :LNB, and the relation

$$3e^{(1.759-R_1)/0.37} + 3e^{(1.759-R_2)/0.37} = +3 \tag{8}$$

in the case of Fe^{3+} :LNB. In Fig. 8, the possible (R_1, R_2) couples satisfying Eqs. (7) and (8) are plotted as solid lines. It can be observed that the distances obtained by EXAFS (squares in Fig. 8) are fully consistent with the bond valence model, thus further corroborating our experimental findings.

IV. *AB INITIO* CALCULATIONS

Having obtained a reliable picture for the local structure of the Fe-polaron defect, we are now in the position to set up a computational model capable of reproducing the measured features. Here the main goal is to achieve a similar accuracy as that probed by EXAFS (i.e., bond length differences of a few hundredth of angstrom between different charge states). To this aim, in a first step we investigated the effect of several computational parameters on the calculated structural properties of ferroelectric $LiNbO_3$ (space group $R3c$) and corundum-type α-Fe_2O_3 (hematite, space group $R\bar{3}c$). Subsequently, the case of the Fe defect in LNB is considered and the calculations are further refined in order to obtain the best agreement with experimental results.

A. Computational parameters

First-principles total-energy calculations have been performed within the spin-polarized DFT as implemented in the Vienna *ab initio* simulation package VASP [53]. A number of valence electron equal to three per atom for lithium ($1s^2\ 2s^1$), 13 for niobium ($4s^2\ 4p^6\ 4d^4\ 5s^1$), six for oxygen ($2s^2\ 2p^4$), and eight for iron ($3d^7\ 4s^1$) was used if not otherwise specified. Nuclei and remaining core electrons were treated within the pseudopotential approach using the projector-augmented wave method [54].

In a first step, several local and hybrid exchange-correlation functionals have been tested using bulk $LiNbO_3$ as model system (see Appendix 1). Thereby, hybrid-functional calculations are performed using the HSE06 functional [55,56], where 25% of the local PBE exchange is substituted by exact exchange. Due to the overall satisfactory agreement with the experimental results and the moderate computational cost, the iron doping is modeled within the generalized gradient approximation (GGA). The results reported in this paper are obtained with the semi-local form proposed by Perdew and Wang (PW91 [57]). The interpolation scheme of Vosko, Wilk, and Nusair [58] was used for the correlation part of the exchange correlation functional. Electronic wave functions were expanded in a plane wave basis containing waves up to a kinetic energy of 400 eV. Gamma centered $8 \times 8 \times 8$,$6 \times 6 \times 6$, and $3 \times 3 \times 3$ k-point meshes [59] were used to carry out the integration in the Brillouin zone of bulk hematite (α-Fe_2O_3), lithium niobate ($LiNbO_3$) and of the Fe-doped lithium niobate supercells described in the following, respectively. Both the plane wave cutoff and the k-point meshes have been proven to yield converged results. The atomic positions were relaxed until the Hellmann-Feynman forces acting on each atom were lower than 0.01 eV/Å.

Transition metals such as Fe and Nb contain d electrons, which are characterized by a strong on-site Coulomb repulsion. The proper treatment of such strongly correlated electrons within DFT is typically problematic. Rollmann *et al.* [60] and Nahm and Park [61] pointed out the importance of a description beyond the mean field theory for the $4d$ and $5d$ electrons of Fe and Nb atoms in hematite and lithium niobate, respectively. In these works, the authors employed the approach commonly referred to as the DFT + U method. This consists in the introduction of a strong intra-atomic interaction in a (screened)

Hartree-Fock like manner, as an on-site replacement of the L(S)DA [62]. In our work, we make use of the simplified approach to the DFT+ U method introduced by Dudarev *et al.* [63]. Within this approach, the rotationally invariant DFT + U functional is described by

$$E_{\mathrm{DFT+U}} = E_{\mathrm{DFT}} + \frac{U-J}{2}\sum_{\sigma}\mathrm{Tr}(\rho^{\sigma} - \rho^{\sigma}\rho^{\sigma}), \qquad (9)$$

where ρ^{σ} is in our case the on-site density matrix of the d electrons of spin σ and

$$\rho^{\sigma} - \rho^{\sigma}\rho^{\sigma} = \sum_{i}\varepsilon_i^{\sigma} - \left(\varepsilon_i^{\sigma}\right)^2. \qquad (10)$$

The sum runs over all the eigenvalues ε_i of the on-site occupancy matrix ρ^{σ}. U is the spherical averaged Hubbard parameter representing the Coulomb interaction and J the screened exchange energy. J is an approximation of the Stoner exchange parameter [64] and nearly equal to 1 eV. In Dudarev's approach the parameters U and J do not enter separately, only the difference $U' = U - J$ is meaningful. As customary [60], we will keep the parameter J constant for all calculations (J =1), so that changes in U' mirror changes in the on-site Coulomb repulsion.

In the limiting case of idempotent on-site occupation $(\rho^{\sigma})^2 = \rho^{\sigma}$ (i.e., ε_i either 0 or 1), the functional (9) coincides with the DFT energy functional. Thus, the second term in the DFT + U functional can be thought of as a penalty function to the DFT total energy expression that forces the on-site occupancy matrix in the direction of idempotency. As a result, localized occupied d orbitals are shifted to lower energies, while empty d orbitals are raised to higher energies proportionally to U' [62].

B. Iron doping in LNB

The accuracy of different XC functionals, as well as the choice of the electronic states to be considered as valence states has been tested on ferroelectric $LiNbO_3$ and α-Fe_2O_3. The results are shown and discussed in the appendix. Due to the somewhat better agreement with the experiment of GGA-PW91 than other functionals, we will perform all the following calculations within this parametrization of the GGA. Thereby the Li $1s^2$ and $2s^1$, the Nb $3s^2$, $3p^6$, $4d^4$ and $5s^1$ as well as the O $2s^2$ and $2p^4$ electrons are considered valence electrons. The chosen number of projectors is thus higher than in our previous works [8,9,65,66].

The values of U', which are best suited for the modeling of $LiNbO_3$ and α-Fe_2O_3, have been determined to be $U'_{\mathrm{Nb}} = 4$ and $U'_{\mathrm{Fe}} = 3$, respectively. However, as the Coulomb repulsion depends on the screening and on the spatial extension of the wave functions, the U values are system dependent. For this reason, the Fe doping is modeled with $U'_{\mathrm{Nb}} = 3{,}4$ and $U'_{\mathrm{Fe}} = 3{,}4{,}5$. Fe ions are modeled as isolated defects in otherwise ideal stoichiometric $LiNbO_3$. Eventual interactions with intrinsic defects or defect clusters necessary to maintain the overall charge balance [26] are not considered in this work. The isolated Li substitutionals are modeled by rhombohedral cells of 2854.85 Å^3 containing 270 atoms, which corresponds to an iron concentration of $\sim 3.5 \times 10^{20}$ atoms/cm^3 or 1.8 mol %. This concentration is very similar to the Fe concentration of 1 mol % of the melt from which the samples described in Sec. II were grown.

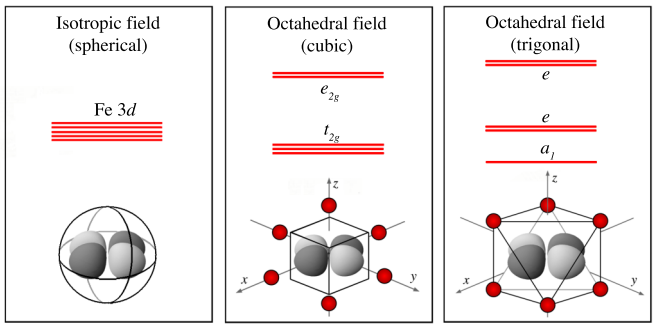

FIG. 9. (Color online) Splitting of the Fe 3d states within different environments. The energetic ordering of the states depends on the orientation of the d orbitals with respect to the oxygen ligands.

According to the strategy discussed in Sec. I, we will only investigate Fe_{Li} substitutionals with valence states 2+ and 3+. The relative stability of defects with different valence states or at other lattice locations is not object of this investigation. Fe_{Li}^{3+} and Fe_{Li}^{2+} are modeled removing the appropriate number of electrons from the electrically neutral supercell containing the Fe_{Li} substitutional. The energetically highest occupied electronic states originate from the Fe 3d shell. These states are well localized around the Fe ion. Therefore subtracting/adding electrons from/to the system corresponds to modifying the valence state of the Fe_{Li} substitutional.

Fe ions at the Li lattice site are octahedrally coordinated with oxygen ligands. The octahedral field lifts the degeneracy of the atomic Fe d states. d orbitals pointing directly at ligands experience more electrostatic repulsion and are shifted to higher energies, while d orbitals pointing between the ligands are less affected by electrostatic repulsion. According to the crystal field theory, a perfect octahedral field (e.g., as in ideal cubic perovskites) splits the d states into a triple-degenerated t_{2g} and double-degenerated e_g levels (see Fig. 9, middle panel). Ferroelectric lithium niobate is a noncentrosymmetric trigonal crystal with tilted oxygen octahedra. This affects the Fe-ligand distances and ligand-Fe-ligand angles, and results in splitting the Fe d states into a singly degenerated a_1 and two double degenerated e levels (see Fig. 9, right panel).

The d electrons can be distributed in different ways among the levels in Fig. 9, middle panel. The levels can be doubly filled with electrons of opposite spin according to their energetic ordering (low spin case or strong field situation). However, if pairing two electrons on the same level becomes energetically too costly, higher energetic levels might be occupied with electrons of the same spin (high spin case or weak field situation). All possible spin configurations have been modeled within our DFT + U models. Independently from the values of U', the high spin configurations turn out to be energetically favored, both for the Fe_{Li}^{3+} and for the Fe_{Li}^{2+} substitutionals.

Within this configuration, in Fe_{Li}^{3+} 5 spin-up and 0 spin-down electrons are distributed among the Fe-3d states. The magnetization is $m = 5$, the electronic configuration Fe=[Ar] $3d^5$ $4s^0$ and the effective charge with respect to the isolated Fe ion is +3. In Fe_{Li}^{2+}, 5 spin-up and one

spin-down electrons are distributed among the Fe-3d states. The magnetization is $m = 4$, the electronic configuration Fe=[Ar] $3d^6$ $4s^0$ and the effective charge with respect to the isolated ion is +2. The resulting electronic structure calculated for $U'_{Nb} = 4$ and $U'_{Fe} = 4$ is shown in Fig. 10. In Fe^{3+}_{Li}, all the spin up d states are occupied. The highest e state is a shallow level close to the valence-band maximum (VBM), while the further a_1 and e levels are in the valence band. All the spin-down d states on the contrary are empty, and the corresponding electronic levels close to the conduction-band minimum (CBM). Thereby the a_1 and one e states are nearly degenerated. All the iron-induced states show almost no dispersion and are extremely localized.

The Coulomb repulsion upon electron capture shifts all electronic levels upwards in Fe^{2+}_{Li}. Again, all spin up d states are occupied, with the highest e state still close to the VBM, even higher than in the Fe^{3+}_{Li} case. One spin down electron is now hosted in the a_1 level shown in Fig. 10, while the empty e electronic states are shifted upwards in the conduction band. This picture is qualitatively the same for all the considered U' values, even if the precise position of the gap levels depends on U'_{Fe}.

The results of the calculations for the structural parameters of the Fe^{3+}_{Li} and Fe^{2+}_{Li} defects in LNB, obtained using the different values of U' are reported in Table II and compared with experimental data obtained in Sec. III. In this case, we used the values obtained at 30 K as they are the closest to the conditions assumed in the computational model (0K). The remaining temperature difference is most probably not important because, as already observed, the experimental results point out that the structural parameters are weakly dependent on T. The relative mismatch between experiment and calculation for the Fe-O_1 and Fe-O_2 distances is about 1% both for Fe^{3+}_{Li} and Fe^{2+}_{Li} for all the choices of the U' parameters. In particular, the calculation reproduces correctly the large lattice relaxation (LLR) of the oxygen ligands associated to the electronic capture at the Fe center, and can be interpreted as the lattice relaxation associated to the polaron formation. Again, the calculated average Fe-O distance (about 2.04 Å for Fe^{3+}_{Li}) is shorter than the average Li-O distance in $LiNbO_3$, calculated in about 2.14 Å. Both these results are in agreement with ours and published data.

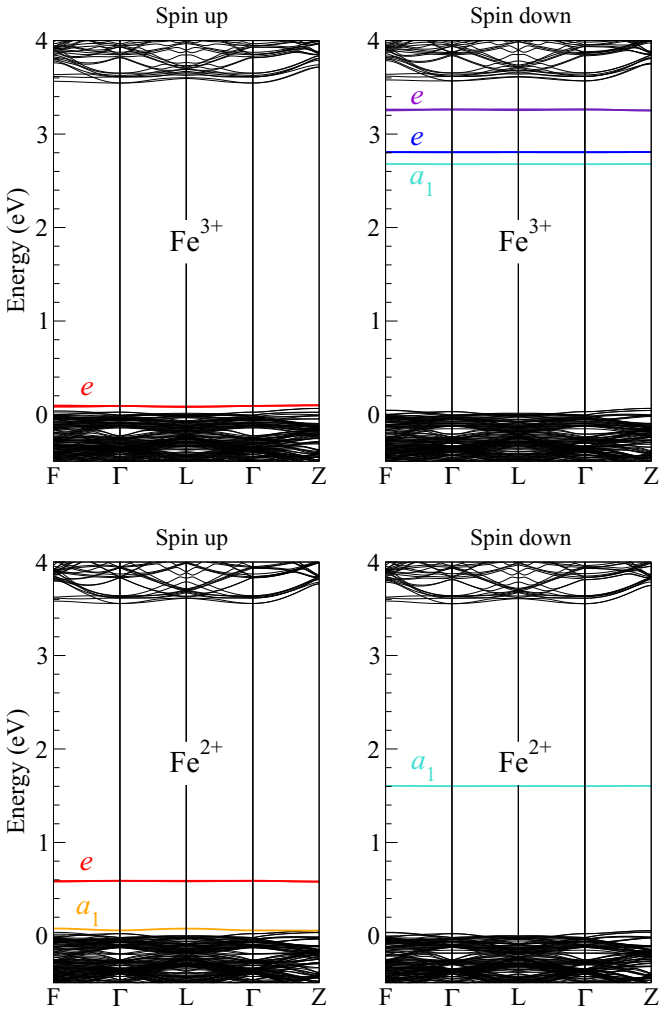

FIG. 10. (Color online) Electronic band structure of the supercells modeling the Fe^{3+}_{Li} (top) and the Fe^{2+}_{Li} substitutional (bottom) calculated with $U'_{Nb} = 4$ and $U'_{Fe} = 4$. Fe induced localized band gap states are plotted in red (spin up) or blue (spin down).

V. DISCUSSION AND CONCLUSIONS

The precise experimental determination of the local structure of the Fe center in both its valence states gives a direct

TABLE II. Structural parameter characterizing the Fe^{2+}_{Li} and Fe^{3+}_{Li} substitutionals calculated for different values of U'. All length in angstroms, Δz labels the displacement of the Fe ions along the [111] crystal axis with respect to the substituted Li. Δ Fe-O is the difference between short and long Fe-O bonds, while Δ Avg. is the difference of the average Fe-O distances in Fe^{2+}_{Li} and Fe^{3+}_{Li}. Experimental data refer to the values obtained by the FEFF-FEFFIT method at 30 K.

U'		Δz Fe	Fe-O_1	Fe-O_2	Avg. Fe-O	Δ Fe-O	Δz Fe	Fe-O_1	Fe-O_2	Avg. Fe-O	Δ Fe-O	Δ Avg.
Nb 4d	Fe 3d			Fe^{2+}_{Li}					Fe^{3+}_{Li}			
3	3	0.1220	2.0519	2.1823	2.1174	0.1298	0.0790	1.9617	2.1194	2.0410	0.1557	0.0764
3	4	0.0893	2.0562	2.1906	2.1226	0.1361	0.0895	1.9645	2.1095	2.0370	0.1450	0.0856
3	5	0.0762	2.0564	2.1960	2.1262	0.1396	0.0992	1.9663	2.1006	2.0335	0.1343	0.0927
4	3	0.1140	2.0546	2.1896	2.1221	0.1350	0.0809	1.9583	2.1358	2.0471	0.1775	0.0750
4	4	0.0970	2.0553	2.1988	2.1271	0.1435	0.1018	1.9647	2.1158	2.0403	0.1511	0.0868
4	5	0.0849	2.0573	2.2033	2.1303	0.1460	0.1124	1.9668	2.1052	2.0360	0.1384	0.0943
Exp. @ 30 K			2.080 ±0.011	2.167 ±0.019	2.124 ±0.011	0.087 ±0.022		1.977 ±0.022	2.071 ±0.022	2.024 ±0.016	0.094 ±0.031	0.100 ±0.019

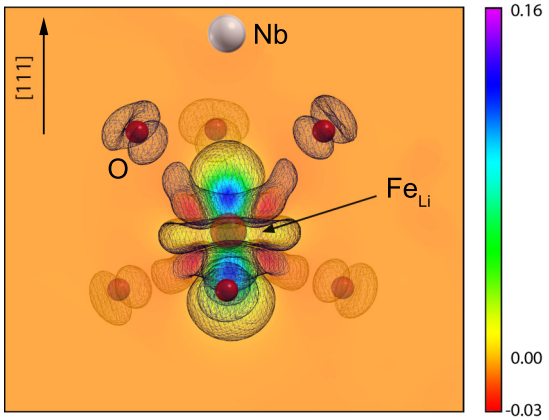

FIG. 11. (Color online) Electronic charge difference $Fe^{2+}_{Li} - Fe^{3+}_{Li}$ calculated with $U'_{Nb} = 4$ and $U'_{Fe} = 4$. The electron captured upon $Fe^{3+}_{Li}/Fe^{2+}_{Li}$ transition is completely localized around the Fe ion, as expected for a small bound polaron. The charge distribution strongly resembles the atomic Fe d_{z^2} orbitals, suggesting a scarce hybridization of such states.

evidence of the polaronic effect: when Fe^{3+} captures an electron and becomes Fe^{2+} the oxygen octahedron expands as described in the phenomenological picture. Using these data in conjunction with the structural data on LNB and hematite, an accurate *first-principles* calculation has been set up. The proposed computational scheme is able to reproduce satisfactorily all the available experimental data, so that we can now use it to depict those features of the Fe polaron which are not directly accessible from experiments.

Figure 11 shows the electronic charge associated with the occupied spin down a_1 state in Fe^{2+}_{Li}, i.e., the electron captured to form the small bound polaron. The electronic charge is strongly localized around the Fe ion and closely resembles the atomic Fe d_{z^2} orbitals, suggesting a scarce hybridization of such states. This setting is consistent with the small bound Fe polaron predicted by Schirmer *et al.* [10]. Furthermore, it is clearly seen that the atomic orbitals point along the [111] crystal axis and thus between the oxygen ligands. This explains why, according to the crystal field theory, the d_{z^2} orbitals experiences less electrostatic repulsion and are more stable (lower energy) than d orbitals pointing directly at ligands. Upon formation of Fe_{Li} substitutionals, the Fe ion is shifted upwards along the [111] crystal axis by about 0.09 Å with respect to the substituted Li, while the surrounding oxygen cages shrinks by an amount which depends on the Fe charge state. As the structural changes occur along the crystal symmetry axis or symmetrically around it, the threefold symmetry is preserved. This corroborates *a posteriori* the assumptions used in the analysis of the EXAFS data. This LLR is similar to the behavior calculated by Nahm and Park for the Nb_{Li} substitutionals. Note that this finding is relevant for the quantitative analysis of the photogalvanic properties of the Fe center because, as described in Ref. [11], the microscopic onset of the photocurrent is triggered by the distances along the z axis of the Fe center from the neighboring Nb ions.

The Fe electronic states localized in the gap are responsible for the optical properties of the iron-doped samples. In particular, the spin-down electron in Fe^{2+}_{Li} might be excited to several levels, according to the picture of Schirmer *et al.* [10], which ascribe to this kind of transitions the large high-energy tails of the polaron absorption band. The electronic charge transition $Fe^{3+}_{Li}/Fe^{2+}_{Li}$ is evaluated within the Slater-Janak transition state model [9,67] at 1.54 eV below the VBM. This value is in excellent agreement with the very similar the value of 1.34 eV calculated by Phillpot and co-workers [26], and with the photoluminescence peak measured at 1.4 eV above the CBM [68].

In conclusion, we have investigated the Fe polaron defect in LNB by combining EXAFS measurements with DFT + U *first-principles* calculations. The experimental analysis allowed to directly observe the structural changes associated to the small Fe polaron presence. The results obtained from two independent data analysis procedures are mutually consistent and the results obtained at different temperatures further confirm the validity of these findings. Using those data and other parameters known from literature, we were able to set up an *ab initio* calculation based on a spin-polarized DFT method which correctly reproduces the experimental data. The best agreement is obtained within a generalized gradient approximation using the PW91 parametrization. In order to catch the finer details of the differences among the long and short Fe-O distances, corresponding to the fact that Fe occupies a noncentrosymmetric position in the oxygen cage, it was also necessary to introduce a Hubbard U correction with a value around 4 eV both for the Nb 4d and the Fe 3d electrons.

Both the experimental and theoretical descriptions are in full agreement with the phenomenological picture of the small polaron formation: when a Fe^{3+} impurity substitues for a Li ion in LNB, the oxygen octahedron is shrinked so that the average metal-oxygen distance is reduced from about 2.16 Å of the Li-O bonds to about 2.03 Å of the Fe-O bonds, a value very similar to the one of Hematite. In this condition the Fe occupies a position which is slightly shifted upwards with respect to the Li site of about 0.1 Å. Whenever an electron is added to the system, it localizes at the Fe site in a configuration very close to the atomic Fe d_{z^2} orbitals causing a partial relaxation of the oxygen cage.

The importance of our findings, beside providing accurate experimental values on the polaron formation process in Fe:LNB, is that we provide an *ab initio* scheme, which could be used to obtain other important information on the polaron defect, such as the different polaron energies and the optical properties of the defect. This approach is therefore complementary to classical theoretical treatment of the polaron defects.

ACKNOWLEDGMENTS

We acknowledge the European Synchrotron Radiation Facility (ESRF) for provision of synchrotron radiation, as well as O. Mathon and the staff of the BM23 beamline for technical assistance. This work has been partially supported by the ESRF Project No. HE-3766. Two of the authors, S.S. and W.G.S., acknowledge the financial support by the Deutsche Forschungsgemeinschaft (DFG) via Sonderforschungsbereich TRR 142 and SCHM1361/21. All the calculations were performed at the Paderborn Center for Parallel Computing (PC^2) and at High Performance Computing Center in Stuttgart

TABLE III. Calculated structural parameters of ferroelectric $LiNbO_3$ obtained with different exchange-correlation functionals and considering different numbers of valence electrons. All distances in Å, the deviations are calculated with respect to the measured values $a_R = 5.494$ Å, $\alpha = 55.867^\circ$ of Ref. [69]. E_g labels the electronic gap (in eV).

Val. Li	Valence Nb	Val. O	XC	LDA $+U$	a_R	Dev.	α	Dev.	Li-O_1	Li-O_2	E_g
$2s^1$	$3p^6\,4d^4\,5s^1$	$2s^2\,2p^4$	LDA	$U' = 0$	5.4220	−1.33%	55.612°	−0.46%	1.9781	2.1991	3.4149
			LDA	$U' = 4$	5.4468	−0.86%	55.656°	−0.38%	1.9572	2.2604	3.4402
			PW91	$U' = 0$	5.5086	+0.27%	55.586°	−0.50%	2.0185	2.2440	3.4431
			PW91	$U' = 4$	5.5234	+0.54%	55.716°	−0.27%	1.9938	2.3091	3.3862
			PBE	$U' = 0$	5.5007	+0.12%	55.563°	−0.54%	2.0103	2.2399	3.4922
			PBE	$U' = 4$	5.5153	+0.39%	55.692°	−0.31%	1.9849	2.3061	3.4247
			HSE06	$U' = 0$	5.4588	−0.64%	55.753°	−0.20%	2.0029	2.2201	5.0291
$2s^1$	$3s^2\,3p^6\,4d^4\,5s^1$	$2s^2\,2p^4$	LDA	$U' = 0$	5.3702	−2.31%	55.711°	−0.28%	1.9685	2.1853	3.5813
			LDA	$U' = 4$	5.3950	−1.83%	55.763°	−0.19%	1.9554	2.2398	3.6362
			PW91	$U' = 0$	5.4770	+0.31%	55.666°	−0.36%	2.0199	2.2366	3.5734
			PW91	$U' = 4$	5.4837	+0.19%	55.850°	−0.03%	2.0061	2.2914	3.5307
			PBE	$U' = 0$	5.4672	−0.49%	55.689°	−0.32%	2.0151	2.2344	3.6454
			PBE	$U' = 4$	5.4735	−0.37%	55.829°	−0.07%	1.9938	2.2925	3.5984
			HSE06	$U' = 0$	5.4139	−1.48%	55.742°	−0.22%	2.0025	2.2100	5.2487
$1s^2\,2s^1$	$3s^2\,3p^6\,4d^4\,5s^1$	$2s^2\,2p^4$	LDA	$U' = 0$	5.4182	−1.40%	55.743°	−0.28%	2.0018	2.2136	3.4816
			LDA	$U' = 4$	5.4364	−1.06%	55.839°	−0.05%	1.9823	2.2784	3.5088
			PW91	$U' = 0$	5.4811	−0.24%	55.716°	−0.27%	2.0343	2.2273	3.5736
			PW91	$U' = 4$	5.4875	−0.12%	55.898°	+0.05%	2.0213	2.2787	3.5309
			PBE	$U' = 0$	5.5405	+0.85%	55.751°	−0.21%	2.0769	2.2627	3.5594
			PBE	$U' = 4$	5.5364	+0.77%	55.994°	+0.23%	2.0504	2.3283	3.4470
			HSE06	$U' = 0$	5.4788	−0.28%	55.823°	−0.09%	2.0605	2.2393	5.1510

(HLRS). Funding from the Progetto di Ateneo CPDA120359 of the University of Padova is also gratefully acknowledged.

APPENDIX

1. Bulk LNB

Table III shows the calculated ground state structural parameters of bulk ferroelectric $LiNbO_3$ obtained considering a different number of valence electrons and different exchange-correlation functionals. The lattice parameters a_R and α are defined in Fig. 12. The noncentrosymmetric structure of ferroelectric $LiNbO_3$ results in two different Li-O bond lengths, which are labeled by Li-O_1 and Li-O_2 in Table III.

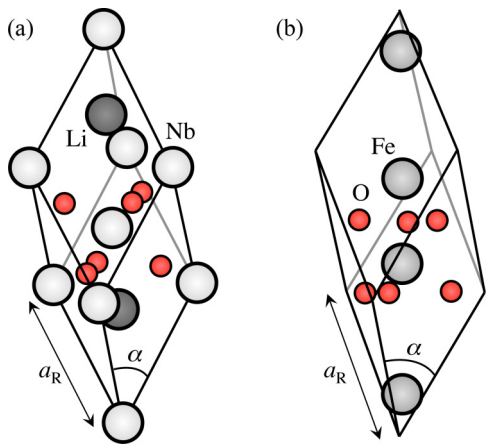

FIG. 12. (Color online) Rhombohedral primitive cells of (a) $LiNbO_3$ and (b) α-Fe_2O_3. Li and Nb atoms in lithium niobate and Fe atoms in hematite are coordinated octahedrally by six O atoms.

The results of this systematic survey are compared with published data [69]. As expected LDA underestimates, while GGA often slightly overestimates the lattice parameters. The slight underestimation within GGA observed here occasionally might be due to the fact that the measurements by Weis and Gaylord [69] are performed at finite (ambient) temperature, while our calculations model $T = 0$ conditions. Nonetheless, an overall very good agreement between theory and measurement is shown, irrespective of the XC functional, with the only exception of LDA, which underestimates the lattice constant a_R by 2.3%.

HSE06 calculations yield lattice constants a_R underestimating the experimental value between 0.28% and 1.48%, depending on the choice of the electrons, which are treated as valence states. Thus hybrid-functional calculations do not significatively improve the agreement with the measured the lattice parameters with respect to classic XC functionals. However, the main benefit of hybrid DFT lies in the more refined description of the electronic structure, as it allows to overcome the known deficits of (semi)local XC functionals leading to a underestimation of the electronic band gaps in most semiconductors. Indeed, the application of hybrid potentials leads to a Γ-band-gap opening of about 1.6 eV with respect to the value calculated within DFT-PBE. The dispersion of the electronic states (not shown in this work) is not affected by the hybrid functionals. Both findings are agreement with similar calculations presented in Ref. [8]. The calculated HSE06 fundamental band gap of 5.03–5-25 eV, is very close to the value calculated in Ref. [70] including quasiparticle corrections calculated within the GW approximation. Though the calculated DFT band gap (3.42 to 3.58 eV, depending on the computational parameters) seems to be in very good agreement with the experimental value of 3.78 eV [71],

TABLE IV. Effect of the $+U$ corrections on the ferroelectric $LiNbO_3$ structural parameters obtained with PBE and PW91 exchange-correlation functionals. All distances in Å, the deviations are calculated with respect to the measured values $a_R = 5.494$ Å, $\alpha = 55.867°$ of Ref. [69]. Δ labels the Li-O_1 − Li-O_2 mismatch and E_g the electronic gap (in eV).

XC	LDA $+U$	a_R	Dev.	α	Dev.	Li-O_1	Li-O_2	Δ	Avg. Li-O	E_g
PBE	$U' = 0$	5.5405	+0.85%	55.751°	−0.21%	2.0769	2.2627	0.1858	2.1698	3.5594
PBE	$U' = 2$	5.5385	+0.81%	55.900°	+0.06%	2.0678	2.2976	0.2298	2.1827	3.4620
PBE	$U' = 3$	5.5378	+0.80%	55.963°	+0.17%	2.0606	2.3095	0.2489	2.1850	3.4367
PBE	$U' = 4$	5.5364	+0.77%	55.994°	+0.23%	2.0504	2.3283	0.2779	2.1894	3.4470
PBE	$U' = 5$	5.5408	+0.85%	56.050°	+0.33%	2.0460	2.3500	0.3040	2.1980	3.4829
PBE	$U' = 6$	5.5444	+0.92%	56.073°	+0.37%	2.0388	2.3725	0.3337	2.2056	3.5510
PW91	$U' = 0$	5.4811	−0.24%	55.716°	−0.27%	2.0343	2.2273	0.1930	2.1308	3.5736
PW91	$U' = 2$	5.4776	−0.30%	55.864°	−0.01%	2.0260	2.2502	0.2242	2.1381	3.5256
PW91	$U' = 3$	5.4789	−0.27%	55.987°	+0.22%	2.0220	2.2624	0.2404	2.1422	3.5242
PW91	$U' = 4$	5.4875	−0.12%	55.898°	+0.05%	2.0213	2.2787	0.2574	2.1500	3.5309
PW91	$U' = 5$	5.4838	−0.19%	55.948°	+0.15%	2.0135	2.2890	0.2755	2.1512	3.5917

closer inspection shows that apparent agreement is due to the high exciton binding energy in $LiNbO_3$. A thorough discussion concerning the fundamental band gap in $LiNbO_3$ can be found in Ref. [70]. Thus HSE06 calculations are in good agreement with the experimental values of the lattice parameters and predict an electronic structure very close to the outcome of more sophisticated (and more computationally costly) GW calculations. Unfortunately, structural relaxations within hybrid functionals are currently not feasible for the supercells with several hundred atoms used to model the iron doping. In order to account for the underestimation of the electronic wave functions localization of the Nb 4d orbitals typical of (semi)local XC functionals, the DFT + U approach is a more convenient alternative.

Table III shows that introducing the Hubbard-like term in the density functional increases the difference between Li-O_1 and Li-O_2 distances. For the DFT + U calculations reported in Table III, we have used the U' value for the Nb d shell of 4 eV suggested in Ref. [61]. However, it is interesting to observe the effect of the strength of the penalty function in Eq. (9) on the $LiNbO_3$ structural parameters. As GGA shows smaller deviations from the experimental values than LDA, we only consider these potentials for further investigations. The corresponding calculations are compiled in Table IV.

The effect of the $+U$ corrections on the structural parameter of $LiNbO_3$ is moderate. The lattice constant a_R is modified by the Hubbard term within the considered range 0-6 eV by no more than 0.15%. Similarly to the outcome of the DFT + U calculations of Rollmann [60], the structural parameters do not show a monotonic behavior with increasing U' values. However, the difference Δ between the two Li-O bond length linearly increases with the strength of the Hubbard correction. This suggests a role of the Nb 4d orbitals in the (mainly covalent) Nb-O bond, with consequent influence on the (mainly ionic) Li-O bond length. In agreement with the work of Nahm and Park [61], we find that experimental results are best reproduced for values of U' of about 4 eV, in particular by using the PW91 exchange-correlation functional. The average Li-O bond length and the difference Li-O_1 − Li-O_2 calculated for this value of U' in 2.150 and 0.257 Å, respectively, are in good agreement with the experimental values of 2.16 and 0.2 Å calculated from published values of Weis and Gaylord [69] (see Fig. 6).

The DFT + U method predicts fundamental band gaps between 3.44 and 3.59 eV, depending on the XC-functional and the U' values. Thus the application of Hubbard potentials has a limited influence on the size of the calculated electronic band gap. This is in agreement with similar calculations in Ref. [61].

2. Hematite

Corundum type α-Fe_2O_3 is an antiferromagnetic insulator at ambient conditions. While hematite has been experimentally described as a charge-transfer insulator, DFT describes it as a Mott insulator with a small band gap. As only models beyond DFT—such as DFT + U or hybrid functionals—are capable to predict hematite as a charge transfer insulator [60,74], only DFT + U or hybrid functional calculations are performed in this study.

As all Fe-ions in hematite are characterized by the same octahedral environment, the magnetic properties at each Fe-site will be identic. However, two types of iron-pairs, characterized by a short and by a large Fe-Fe distance along the [111] crystal axis, can be discriminated (see Fig. 12). This opens the possibility for three different antiferromagnetic configurations. In the magnetic ordering AFM1 (↑↑↓↓) Fe-Fe long pairs have equal magnetic moments, while short Fe-Fe pairs have opposite magnetic moments. The AFM2 ordering (↑↓↑↓) corresponds to Fe chains of alternating spin orientation along the [111] crystal axis. Finally, in the AFM3 configuration (↑↓↓↑) Fe-Fe long pairs have opposite magnetic moments, while short pairs have equal magnetic moments. All possible antiferromagnetic configurations have been modeled within the described DFT + U approach, along with the ferromagnetic (FM) and non magnetic ordering (NM). The results of the calculations are compiled in Table V.

The antiferromagnetic ordering is energetically favored over ferromagnetic and nonmagnetic solutions. Among the antiferromagnetic configurations, the magnetic ordering AFM1 is the most stable. This is in agreement with similar DFT + U calculations by Rollmann *et al.* [60] and previous LCAO calculations by Catti *et al.* [75].

TABLE V. Ground-state structural parameters obtained with the PW91 exchange-correlation functionals in hematite. All distances in angstroms. Energy differences (in eV per primitive cell) are given with respect to the non magnetic configuration. The deviations are calculated with respect to the measured values of Ref. [47]. E_g labels the electronic gap (in eV).

Spin conf.	Fe Spin	ΔE	μ_B	LDA $+U$	a_R	Dev.	α	Dev.	Fe-O_1	Fe-O_2	Fe-Fe (1)	Fe-Fe (2)	E_g
Exp [47].					5.420		55.282°				2.883	3.982	
Exp [72].					5.427		55.280°		1.944	2.113	2.896	3.977	
Exp [73].													2.0–2.7
FM	↑↑↑↑	−6.6050	4.25	$U'=4$	5.4328	+0.2%	55.779°	+0.9%	1.9693	2.1050	2.8519	4.0063	4.2733
AFM1	↑↑↓↓	−7.6892	4.11	$U'=4$	5.4127	−0.1%	55.330°	+0.1%	1.9449	2.1015	2.8600	3.9935	2.7120
AFM2	↑↓↑↓	−7.1333	4.17	$U'=4$	5.4137	−0.1%	55.646°	+0.6%	1.9398	2.1259	2.9069	3.9334	1.9269
AFM3	↑↓↓↑	−7.2987	4.16	$U'=4$	5.3985	−0.4%	55.910°	+1.1%	1.9661	2.0842	2.8183	3.9905	2.0955
NM		0.0000	0.00	$U'=4$	5.0259	−7.8%	58.311°	+5.5%	1.9265	1.9181	2.2414	3.9905	0.4606
AFM1	↑↑↓↓		3.88	$U'=2$	5.4142	−0.1%	55.080°	−0.4%	1.9302	2.1132	2.8912	3.9757	1.9509
AFM1	↑↑↓↓		4.01	$U'=3$	5.4153	−0.1%	55.191°	−0.2%	1.9397	2.1078	2.8770	3.9863	2.3455
AFM1	↑↑↓↓		4.11	$U'=4$	5.4127	−0.1%	55.330°	+0.1%	1.9449	2.1025	2.8600	3.9935	2.7120
AFM1	↑↑↓↓		4.20	$U'=5$	5.4083	−0.2%	55.364°	+0.2%	1.9479	2.0945	2.8461	4.0003	3.0050
AFM1	↑↑↓↓		4.29	$U'=6$	5.4000	−0.4%	55.419°	+0.3%	1.9498	2.0865	2.8292	4.0043	3.3960
HSE06	↑↑↓↓		4.12		5.3974	−0.4%	55.361°	+0.1%	1.9287	2.0968	2.8698	3.9401	4.0504

HSE06 calculation of the AFM1 spin configuration predicts lattice parameters and magnetic moments which closely mirror the measured values [60] (see Table V). However, the electronic band gap is overestimated by more than 1 eV. This is in agreement with previous calculations by Canepa *et al.*, which explain the deviation from the experiment by the overlocalization of the 3*d* electrons on the iron atoms [74]. In order to achieve agreement with the measured gaps, hybrid functionals with exact-exchange percentages between 9% and 10% have to be considered [74].

An alternative approach that allows to model structural, electronic and magnetic properties of α-Fe_2O_3 in agreement with measured values is the DFT $+ U$ method, provided, the correct U' magnitude is chosen [60,74]. In the lower part of Table V, we show the dependence of different structural properties on the U' value. While the on-site Hubbard correction stabilizes the magnetic moment, we observe a minor influence on the structural properties. Cell size and symmetry barely change for U' values in the range 2–6 eV. Concerning the internal parameters, the mismatch between the Fe-O_1-Fe-O_2 bonds shrinks for higher values of the Hubbard U. On the contrary, the difference between short and long Fe-Fe bonds grows with U'. Independently from the U' value, the calculated structural parameters are in fairly good agreement with available experimental data. However, in further agreement with Rollmann and co-workers, we find that the best overall agreement is achieved for $U' = 3$. In particular, the calculated average Fe-O distance of 2.024 Å is in perfect agreement with the value of ∼2.03 Å of Refs. [47,48]. The electronic band gap of 2.35 eV calculated for this U' value is within experimental range 2.0–2.7 eV [73].

[1] J. Ashley, M.-P. Bernal, G. W. Burr, H. Coufal, H. Guenther, J. A. Hoffnagle, C. M. Jefferson, B. Marcus, R. M. Macfarlane, R. M. Shelby, and G. T. Sincerbox, IBM J. Res. Develop. **44**, 341 (2000).

[2] P. Guenther and P. Huignard, *Photorefractive Materials and their Applications 2* (Springer, Berlin, 2006), Chap. 4, pp. 96–100.

[3] D. Kip, Appl. Phys. B **67**, 131 (1998).

[4] M. Stock and S. Dunn, IEEE Trans. Ultras. Ferroelectr. Freq. Control **58**, 1988 (2011).

[5] M. Stock and S. Dunn, J. Phys. Chem. C **116**, 20854 (2012).

[6] T. Volk and M. Wöhlecke, *Lithium Niobate: Defects, Photorefraction and Ferroelectric Switching*, edited by R. Hull, R. M. Osgood Jr., J. Parisi, and H. Warlimont, Springer Series in Material Science Vol. 115 (Springer-Verlag, Berlin, 2008), Chap. 2, pp. 9–30.

[7] A. Yariv, S. S. Orlov, and G. A. Rakuljic, J. Opt. Soc. Am. B **13**, 2513 (1996).

[8] Y. Li, W. G. Schmidt, and S. Sanna, Phys. Rev. B **89**, 094111 (2014).

[9] Y. Li, S. Sanna, and W. G. Schmidt, J. Chem. Phys. **140**, 234113 (2014).

[10] O. F. Schirmer, M. Imlau, C. Merschjann, and B. Schoke, J. Phys.: Condens Matter **21**, 123201 (2009).

[11] O. F. Schirmer, M. Imlau, and C. Merschjann, Phys. Rev. B **83**, 165106 (2011).

[12] D. Emin, *Polarons* (Cambridge University Press, Cambridge, 2013), Chap. 11, pp. 95–118.

[13] I. G. Austin and N. F. Mott, Adv. Phys. **50**, 757 (2001).

[14] H. Wang, X.-Y. Kuang, D. Dong, Y. Xiong, and K.-W. Zhou, Physica B: Condens. Matter **367**, 53 (2005).

[15] T. Gog, P. Schotters, J. Falta, G. Materlik, and M. Grodzicki, J. Phys.: Condens. Matter **7**, 6971 (1995).

[16] H. Sothe and J. M. Spaeth, J. Phys.: Condens. Matter **4**, 9901 (1992).

[17] L. Rebouta, M. F. da Silva, J. C. Soares, M. Hage-Ali,

J. P. Stoquert, P. Siffert, J. A. Sanz-Garcia, E. Diguez, and F. Agull-Lopez, Europhys. Lett. **14**, 557 (1991).
[18] A. Zaltron, N. Argiolas, D. De Salvador, M. Bazzan, M. Ciampolillo, L. Bacci, and C. Sada, NIMB **275**, 11 (2012).
[19] D.-S. Yang, N. Sung, and T. H. Yeom, J. Phys. Soc. Jpn **78**, 114605 (2009).
[20] T. Vitova, J. Hormes, M. Falk, and K. Buse, J. Appl. Phys. **105**, 013524 (2009).
[21] T. S. Bush, C. R. A. Catlow, A. V. Chadwick, M. Cole, R. M. Geatches, G. N. Greaves, and S. M. Tomlinson, J. Mater. Chem. **2**, 309 (1992).
[22] M. Clark, F. DiSalvo, A. M. Glass, and G. E. Peterson, J. Chem. Phys. **59**, 6209 (1973).
[23] M. V. Ciampolillo, A. Zaltron, M. Bazzan, N. Argiolas, and C. Sada, Appl. Spectr. **65**, 216 (2011).
[24] S. A. Basun, T. J. Evans, D. R. Bunning, S. Guha, J. O. Barnes, G. Cook, and R. S. Meltzer, J. Appl. Phys. **92**, 7051 (2002).
[25] M. V. Ciampolillo, A. Zaltron, M. Bazzan, N. Argiolas, C. Sada, and M. Bianconi, J. Appl. Phys. **107**, 084108 (2010).
[26] H. Xu, A. Chernatynskiy, D. Lee, S. B. Sinnott, V. Gopalan, V. Dierolf, and S. R. Phillpot, Phys. Rev. B **82**, 184109 (2010).
[27] H. Kurz, E. Krätzig, W. Keune, H. Engelmann, U. Gonser, B. Dischler, and A. Räuber, Appl. Phys. **12**, 355 (1977).
[28] M. Falk, J. Japs, T. Woike, and K. Buse, Appl. Phys. B **87**, 119 (2007).
[29] E. D. Crozier, J. J. Rehr, and R. Ingalls, *X-ray Absorption*, edited by D. C. Koningsberger and R. Prins (Wiley, New York, 1988) .
[30] P. A. Oday, J. J. Rehr, S. I. Zabinsky, and G. E. Brown, J. Am. Chem. Soc. **116**, 2938 (1994).
[31] P. Fornasini, S. a Beccara, G. Dalba, R. Grisenti, A. Sanson, M. Vaccari, and F. Rocca, Phys. Rev. B **70**, 174301 (2004).
[32] G. N. Greaves, J. Non-Cryst. Sol. **71**, 203 (1985).
[33] G. Bunker, Nucl. Instrum. Methods Phys. Res. **207**, 437 (1983).
[34] P. Fornasini, *Synchrotron Radiation - Basics, Methods and Applications*, edited by S. Mobilio, C. Meneghini, and F. Boscherini (Springer-Verlag, Berlin, 2015), Chap. 6, pp. 181–211.
[35] P. Fornasini, F. Monti, and A. Sanson, J. Synchr. Rad. **8**, 1214 (2001).
[36] K. Olimov, M. Falk, K. Buse, T. Woike, J. Hormes, and H. Modrow, J. Phys.: Cond. Matter **18**, 5135 (2006).
[37] A. Ide-Ektessabi, T. Kawakami, and F. Watt, Nucl. Instrum. Methods Phys. Res. B **213**, 590 (2004).
[38] H. Xu, D. Lee, J. He, S. B. Sinnott, V. Gopalan, V. Dierolf, and S. R. Phillpot, Phys Rev B **78**, 174103 (2008).
[39] J. M. Tranquada and R. Ingalls, Phys. Rev. B **28**, 3520 (1983).
[40] A. L. Ankudinov, B. Ravel, J. J. Rehr, and S. D. Conradson, Phys. Rev. B **58**, 7565 (1998).
[41] M. Newville, B. Ravel, J. J. Rehr, E. Stern, and Y. Yacoby, Physica B **208-209**, 154 (1995).
[42] A. Sanson, O. Mathon, and S. Pascarelli, J. Chem. Phys. **140**, 224504 (2014).
[43] P. Fornasini and F. Rocca, EXTRA *Code for EXAFS Analysis* (University of Trento, Trento, 1998).
[44] J. J. Rehr, C. H. Booth, F. Bridges, and S. I. Zabinsky, Phys. Rev. B **49**, 12347(R) (1994).
[45] H. Wende and K. Baberschke, J. Elect. Spectr. Rel. Phenom. **101-103**, 821 (1999).
[46] M. Newville, P. Līviņš, Y. Yacoby, J. J. Rehr, and E. A. Stern, Phys. Rev. B **47**, 14126 (1993).
[47] L. Pauling and S. B. Hendricks, J. Am. Chem. Soc. **47**, 781 (1925).
[48] A. H. Hill, F. Jiao, P. G. Bruce, A. Harrison, W. Kockelmann, and C. Ritter, Chem. Mater. **20**, 4891 (2008).
[49] G. Dalba, P. Fornasini, M. Grazioli, and F. Rocca, Phys. Rev. B **52**, 11034 (1995).
[50] N. E. Brese and M. O'Keefee, Acta Cryst. **B47**, 192 (1991).
[51] I. D. Brown, Acta Cryst. **B33**, 1305 (1977).
[52] I. D. Brown, *The Chemical Bond in Inorganic Chemistry: The Bond Valence Model*, IUCr Monographs on Crystallography (Book 12) (Oxford University Press, Oxford, 2006).
[53] G. Kresse and J. Furthmüller, Phys. Rev. B **54**, 11169 (1996).
[54] P. E. Blöchl, Phys. Rev. B **50**, 17953 (1994).
[55] J. Heyd, G. E. Scuseria, and M. Ernzerhof, J. Chem. Phys. **118**, 8207 (2003).
[56] A. V. Krukau, A. F. Vydrov, O. A.and Izmaylov, and G. E. Scuseria, J. Chem. Phys. **125**, 224106 (2006).
[57] J. P. Perdew and W. Yue, Phys. Rev. B **33**, 8800(R) (1986).
[58] S. H. Vosko, L. Wilk, and M. Nusair, Can. J. Phys. **58**, 1200 (1980).
[59] H. J. Monkhorst and J. D. Pack, Phys. Rev. B **13**, 5188 (1976).
[60] G. Rollmann, A. Rohrbach, P. Entel, and J. Hafner, Phys. Rev. B **69**, 165107 (2004).
[61] H. H. Nahm and C. H. Park, Phys. Rev. B **78**, 184108 (2008).
[62] V. I. Anisimov, F. Aryasetiawan, and A. I. Lichtenstein, J. Phys.: Condens. Matter **9**, 767 (1999).
[63] S. L. Dudarev, G. A. Botton, S. Y. Savrasov, C. J. Humphreys, and A. P. Sutton, Phys. Rev. B **57**, 1505 (1998).
[64] I. V. Solovyev, P. H. Dederichs, and V. I. Anisimov, Phys. Rev. B **50**, 16861 (1994).
[65] S. Sanna and W. G. Schmidt, Phys. Rev. B **81**, 214116 (2010).
[66] S. Rode, R. Hölscher, S. Sanna, S. Klassen, K. Kobayashi, H. Yamada, W. G. Schmidt, and A. Kühnle, Phys. Rev. B **86**, 075468 (2012).
[67] S. Sanna, T. Frauenheim, and U. Gerstmann, Phys. Rev. B **78**, 085201 (2008).
[68] A. Harhira, L. Guilbert, P. Bourson, and H. Rinnert, Appl. Phys. B **92**, 555 (2008).
[69] R. S. Weis and T. K. Gaylord, Appl. Phys. A **37**, 191 (1985).
[70] A. Riefer, S. Sanna, A. Schindlmayr, and W. G. Schmidt, Phys. Rev. B **87**, 195208 (2013).
[71] A. Dhar and A. Mansingh, J. Appl. Phys. **68**, 5804 (1990).
[72] L. W. Finger and R. M. Hazen, J. Appl. Phys. **51**, 5362 (1980).
[73] R. Zimmermann, P. Steiner, R. Claessen, F. Reinert, S. Hüfner, P. Blaha, and P. Dufek, J. Phys.: Condens. Matter **11**, 1657 (1999).
[74] P. Canepa, E. Schofield, A. V. Chadwick, and M. Alfredsson, Phys. Chem. Chem. Phys. **13**, 12826 (2011).
[75] M. Catti, G. Valerio, and R. Dovesi, Phys. Rev. B **51**, 7441 (1995).